



TECHNICAL ARTICLE

# Precipitation and Flow Behavior of AISI 630 Stainless Steel Deformed at Elevated Temperatures

Z. Sangarimotlagh, B. Tolaminejad, A. Momeni, I. Fedorova, I.S. Zuiko, and R. Kaibyshev

Submitted: 8 April 2022 / Revised: 21 July 2022 / Accepted: 28 July 2022

Hot compression tests were performed on the samples of AISI 630 stainless steel in the temperature range of 900–1050 °C and at strain rates of  $10^{-3}$ – $1\text{ s}^{-1}$ . Single peak stress flow behavior was observed at all deformation conditions. An irregular relationship was found between the peak point of flow curves and processing condition, i.e., temperature and strain rate. The stress relaxation tests at the temperature range of 900–1050 °C revealed that dynamic precipitation (DP) of carbides in the matrix and grain boundaries causes the considered irregularities in the peak stress. The FE-SEM studies also showed that DP of carbides could be responsible for the retardation of dynamic recrystallization (DRX). The phase extraction by residual testing ascertained that fine niobium carbides are the major sources for the effect of DP on the microstructural mechanisms. EBSD and optical microscopy confirmed the occurrence of continuous dynamic recrystallization by the progressive evolution of substructure toward the formation of new small grains. The enhancing rotated (cube) or slight weakening of copper and brass/ Goss texture components were mainly associated with the DRX. The hyperbolic sine equation is used in calculating the activation energy at strain of 0.4 as 485.6 kJ/mol.

**Keywords** AISI 630, constitutive analysis, dynamic precipitation, dynamic recrystallization, hot deformation, stress relaxation

## 1. Introduction

AISI 630 (also known as UNS S17400) is a hardenable martensitic stainless steel (SS) with high strength, acceptable corrosion resistance, proper welding characteristics and relatively good ductility rather than other SSs. Its valuable combination of properties gives designers opportunities to add reliability to their products while simplifying fabrication and often reducing costs. Chemical processing, biomedical, aeronautics, nuclear waste disposal, turbine production and mechanical parts manufacturing are just a few of the fields where it can be used (Ref 1, 2). Hot deformation is a vital forming step in the early stage of processing (Ref 3). The microstructure evolution and flow behavior during hot working are affected by the processing parameters (i.e., strain, strain rate, temperature) as well as nature and type of metals, especially their stacking fault energy (SFE).

The most common softening mechanisms through hot deformation of metals are dynamic recovery (DRV) and dynamic recrystallization (DRX) (Ref 4–7). In low-SFE metals,

DRX nucleation occurs by the discontinuous mechanism (DDRX) in which grain boundary serrations and bulges are formed by the strain-induced boundary migration (SIBM) (Ref 5, 8, 9). Then, the bulged area becomes new grains when they cut from the parent grain. Otherwise, in materials having high SFE values the new DRX grains form by a continuous process (known as CDRX) (Ref 5). In CDRX, the well-developed subgrains initiated by developed DRV, steadily evolve to the new grains, while the misorientation along the boundaries exceeds  $15^\circ$ . Although CDRX generally occurs in high-SFE metals, it can also be an alternative softening mechanism in low-SFE metals, when the conventional DDRX is restricted. DDRX in low-SFE metals is frequently constrained as the grain boundaries are immobilized. Deformation at low temperatures and the formation of fine second-phase particles before or during hot working (dynamic precipitation, DP) are the major reasons which restrict DDRX and propel CDRX (Ref 10).

In materials susceptible to the DP of second phases at hot working temperatures, interactions with DRX occur because both phenomena tend to consume the stored deformation energy (Ref 11). The force applied to the high angle grain boundaries (HAGBs) by the particles effectively pins them and, thus, retards the recrystallization by DDRX (Ref 12, 13). Although the interplay between microalloyed carbides and recrystallization in HSLA steels has been studied successfully (Ref 14), fewer have been published in stainless steels (Ref 15–18). The coexistence of C with carbide forming elements, e.g., Cr, Nb and Ti, makes stainless steels easily affected by the interaction between various types of carbides and grain boundaries. Niobium used in AISI 630 often promotes the formation of NbC instead of  $\text{Cr}_{23}\text{C}_6$  and boosts strength by grain refinement (Ref 19). The possible formation of NbC during hot working indicates that the deformation behavior of AISI 630 is much more complicated than other Nb-free stainless steels. In the current research, hot compression tests

Z. Sangarimotlagh, B. Tolaminejad, and A. Momeni, Materials Science and Engineering Department, Hamedan University of Technology, Hamedan, Iran; I. Fedorova, Department of Physics, Division of Microstructure Physics, Chalmers University of Technology, Gothenburg, Sweden; I.S. Zuiko and R. Kaibyshev, Belgorod National Research University, Belgorod, Russia. Contact e-mail: tolaminejad@hut.ac.ir.

have been conducted to investigate the flow behavior and microstructural evolution in AISI 630 with attention to the precipitation of alloying elements and its effect on the restoration mechanisms.

## 2. Experimental Procedure

### 2.1 Hot Compression Tests and Microstructure Characterization

The chemical composition of the AISI 630 stainless steel used in this investigation is presented in Table 1. The cylindrical specimens with the dimension of  $\phi 10 \times 15$  mm (Fig. 1a) were machined for hot compression tests. Graphite was utilized on the contacting surface between specimen and tooling head to reduce friction. The tests were conducted on the samples with the initial grain size of  $10 \mu\text{m}$  at temperature of 900, 950, 1000 and 1050 °C and strain rates of 0.001, 0.01, 0.1 and  $1.0 \text{ s}^{-1}$ , and the strain of 0.7 (Fig. 1b). The interrupted tests at strains of 0.3 and 0.7 were also analyzed to monitor the influence of strain on the progress of microstructural evolutions. In order to ensure that the temperature distributed homogeneously inside the specimen, the temperature was maintained for 3 min before the compression tests. The samples were rapidly quenched after deformation to retain the microstructures. They were then cut into two halves parallel to the compression axis using wire cutter and optical micrographs were taken from the center point of each sample. For this reason, the samples were mounted and their surface was sandpapered using 100-2500 grit in a standard manner. Afterward, mechanical polishing was done utilizing suspensions of  $0.3 \mu\text{m}$   $\text{Al}_2\text{O}_3$  powder. Eventually, the prepared samples were electrolytically etched in an aqueous reagent of 60%  $\text{HNO}_3$  under the potential of 2 V dc to characterize the old austenite boundaries. Microscopic observations were implemented using Meiji ML7100 optical microscope, and the grain size was determined by the MIP image analysis software. Figure 1(c) represents the initial microstructure of material showing a martensitic structure at the ambient temperature.

Also, FEI Nova NanoSEM 450 FEG-SEM supplied with the EDX and EBSD detectors was employed to better characterize the microstructural evolutions. The samples for EBSD-analysis were electropolished in Struers A2 solution at 25 V for 60 s. TexSEM Labs orientation imaging microscopy software was used to evaluate the raw data.

### 2.2 Stress Relaxation Test

The stress relaxation was carried out to examine the strain-induced precipitation at the hot compression temperatures. Before starting the test, samples were reheated to 1200 °C, held for 10 min and quenched to room temperature. This step was performed to keep all primary carbides into solution. After soaking for 5 min, a primary small strain (5%) was applied to

the samples and then the location of anvils maintained constant. When starting the test, the machine (SANTAM STM5) recorded stress required to keep anvils at the first location. The internal elastic strain gradually changes to the dislocation movement (plastic strain), leading to a gentle decrease in stress. The test was repeated for all deformation temperatures applied in the previous section.

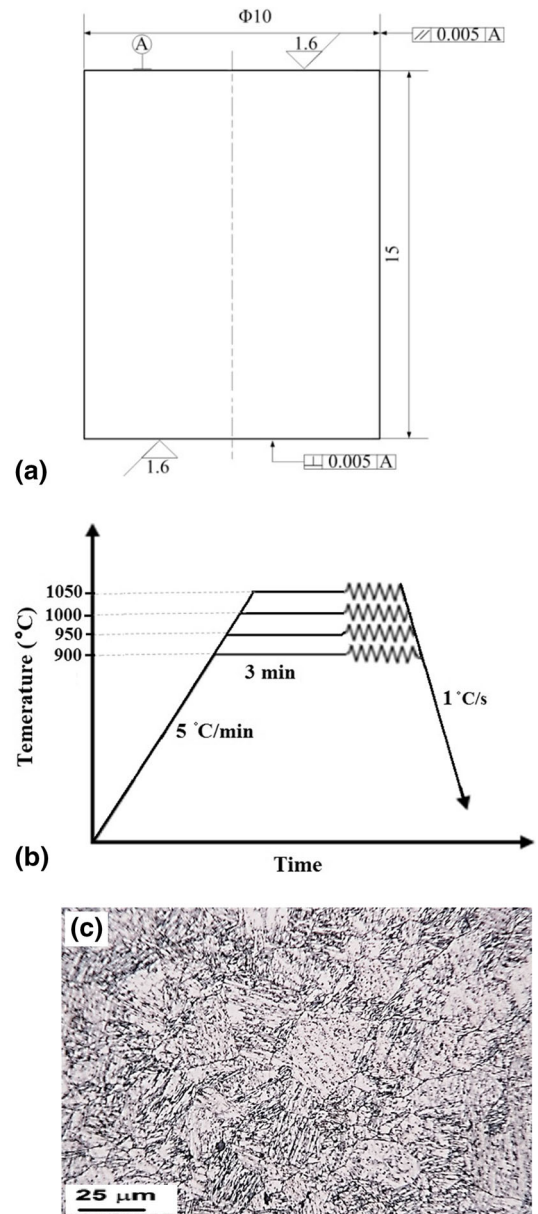


**Fig. 1** (a) Drawing of test sample, (b) schematic of the thermomechanical cycles and (c) initial microstructure of AISI 630 stainless steel

**Table 1** Chemical composition of AISI 630 stainless steel utilized in the present study (all in wt.%)

C	Cr	Ni	Cu	Mn	Si	Nb	Mo	S	Co	W	Fe
0.043	14.8	4.12	3.1	0.67	0.52	0.23	0.35	0.021	0.15	0.03	Rest

### 2.3 Electrolytic Extraction of Precipitated Particles

The type of precipitates in the deformed samples was analyzed by an electrolytic method. A film with 2 mm in thickness of samples at various conditions was prepared. To separate the second-phase particles from the matrix, the film was dissolved into an acidic solution composed of 10% hydrochloric acid, 1% citric acid and methanol. The dissolution of film was carried out in an electrolysis cell, in which a direct power supply with variable voltage and current applied a current density of 0.1% A/cm<sup>2</sup> between the anode (the film) and cathode (platinum). During electrolysis, the precipitates were extracted and filtered for the next step. Finally, the filtered residue was analyzed by XRD (Philips diffractometer model PW1800, Cu K $\alpha$ ) to identify the type of precipitates.

## 3. Results and Discussion

### 3.1 Flow Curves Analysis

**3.1.1 Effect of Strain Rate.** The stress–strain curves at several strain rates are illustrated in Fig. 2. All the flow curves consist of two or more regions. The first region is more controlled by hardening and the flow stress sharply increases up to the peak stress. In this region, DRV also brings about, but with lower rate than work hardening. In the second region, beyond the peak stress, slight flow softening or a plateau (at large strains) is observed. The plateau is introduced when the material is fully recrystallized and the effects of DRX and work hardening are balanced (Ref 5, 20-24).

The results tentatively show that the peak stress (start of DRX) is changed to greater strains and stresses as strain rate

increases (Ref 25). This is attributed to the enhancement of dislocation generation rate and the negative effect on the rate of DRV (Ref 26). However, some atypical positions of the peak have been revealed at 900 °C. The irregularities appear as the unusual increase in the peak strain,  $\epsilon_p$ , at strain rate of 0.001 s<sup>-1</sup>, decrease at 0.01 s<sup>-1</sup> and the next increase at 1 s<sup>-1</sup>. In other words, less recrystallization is expected to occur at the strain rate of 0.001 s<sup>-1</sup> from the abnormal increase in  $\epsilon_p$ . At low strain rates (e.g., 0.001 s<sup>-1</sup>), the long deformation period allow the precipitation of fine carbides by DP, which can delay or even inhibit DRX (Ref 27). This idea has been further studied in Sect. 3.2, 3.3 and 3.4 using detailed microstructural analyses.

**3.1.2 Effect of Deformation Temperature.** When the temperature rises at a given strain rate, the level of flow stress and peak stress decreases (Fig. 2). Due to the increase in the mobility of dislocations and grain boundaries, DRV and DRX are popular at higher deformation temperatures (Ref 28). This easily signifies the lower flow stress and the transfer of peak point to less strains at higher temperatures (Ref 29).

Although one might expect sharper peaks and more steep flow softening at higher temperatures, weaker peaks and flow softening at 950-1050 °C can be found. In addition, the variation of  $\epsilon_p$  with temperature in Fig. 3(a) indicates that  $\epsilon_p$  at 900 °C is unexpectedly lower than that in higher temperatures. These observations further corroborate the idea that the material behaves uncommonly at specific deformation conditions. The hypothesis of interaction between DRX and DP at specific deformation temperatures and strain rates, likely 950-1050 °C and 0.001 s<sup>-1</sup>, can be proposed again to justify the observed irregular behavior.

Since the peak point is actually the starting point of DRX, the observations in Fig. 3(a) imply on the delayed DRX at

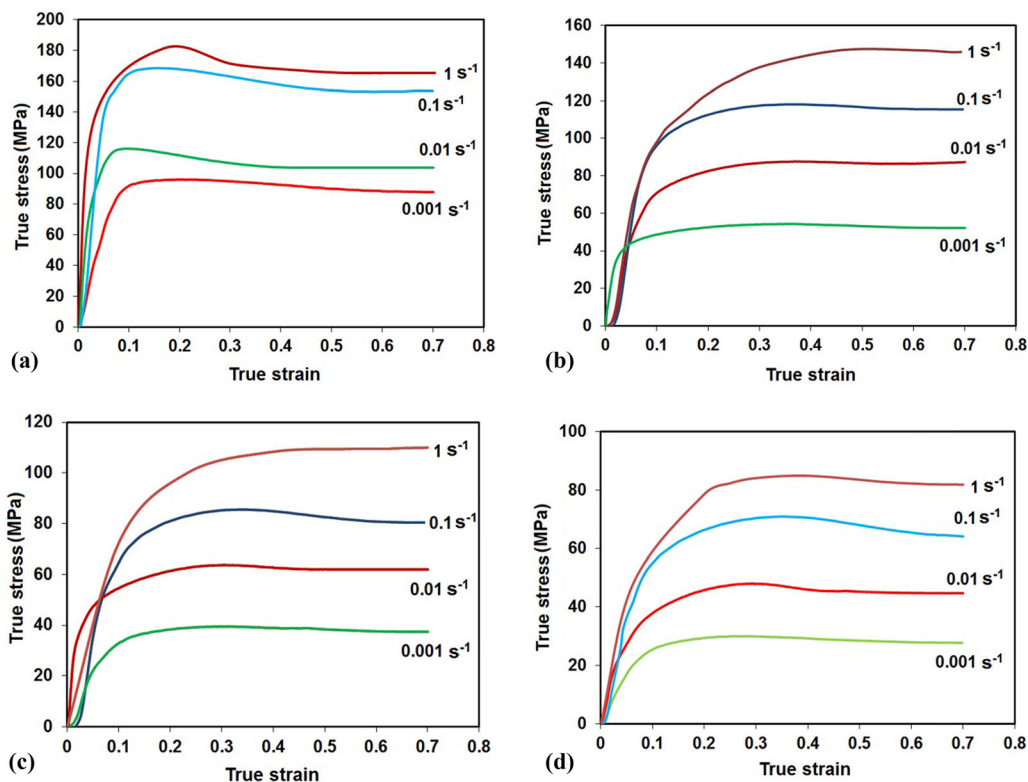


**Fig. 2** Flow curves of AISI 630 stainless steel at different strain rates and temperature of (a) 900 °C, (b) 950 °C, (c) 1000 °C and (d) 1050 °C



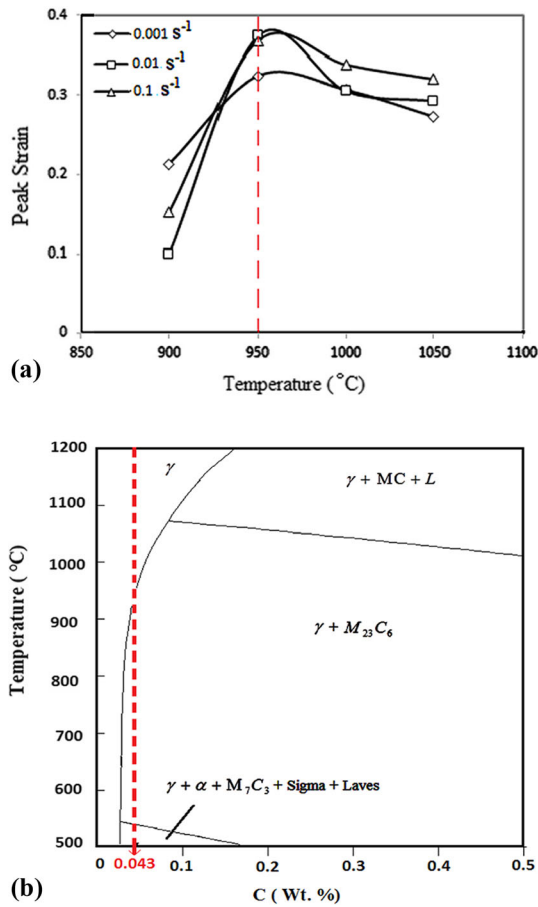


**Fig. 3** (a) Variations of peak strain with temperature at several strain rates and (b) phase diagram of steels with the similar values of alloying elements as Table 1 and different carbon percentage. The location of AISI 630 SS (0.043 wt.% C) is shown by the dashed line

temperatures over 900 °C. It appears that a secondary microstructural mechanism, likely DP, is facilitated at high temperatures, i.e., 950-1050 °C, to occur before and postpone DRX. Although, the increase is expected to occur even at 900 °C, it appears that at 900 °C, DRX precedes DP and it is the reason for the decreased  $\epsilon_p$ . To support this idea further microstructural evidence is presented in the forthcoming sections.

### 3.2 Precipitation Behavior

The phase diagram of similar material (the same values of alloying elements), with various carbon contents, established by the Thermo-Calc program, is presented in Fig. 3(b). The dotted line, indicating the position of AISI 630 (0.043 wt.% C), shows the presence of M<sub>7</sub>C<sub>3</sub> and M<sub>23</sub>C<sub>6</sub> (M = Fe, Cr, Nb, Mo and W) carbides within a matrix of α and γ at low and high temperatures, respectively. However, in non-equilibrium condition it is also possible to obtain the third type of carbide, i.e., MC (M is often Nb and W) in the matrix. Other phases, such as sigma and Laves, are often formed during aging and are absent during normal or fast cooling after post-deformation conditions.

To confirm the above calculations, a piece of deformed samples at 900 and 1050 °C (outside and inside the irregular

behavior region), was dissolved electrolytically according to Sect. 2.3, and the residue was analyzed by the XRD method. The results in Fig. 4 represent the existence of NbC and Cr<sub>15.58</sub>Fe<sub>7.42</sub>C<sub>6</sub> (M<sub>23</sub>C<sub>6</sub>) carbides in the deformed materials, which supports the irregular behaviors in the peak strain, observed in Fig. 2 and 3(a). According to the research by Jonas et al. (Ref 12), Nb and Cr have, respectively, the highest and lowest potential to form carbides effective on the interaction with recrystallization. They have stated that NbC in stainless steels has two important effects: reducing the tendency for the chromium-rich precipitation and pinning the grain boundaries which should contribute to DRX.

Jonas et al. (Ref 12) also reported that coarsening of NbC before or during deformation results in resuming the DRX in Nb-microalloyed steels. The interaction between NbC and DRX often happens at low strain rates, such as 0.001 s<sup>-1</sup>, where there is enough time for DP to start before DRX. At high strain rates, however, as the deformation time is short, enough precipitates for interaction with DRX do not usually form. Moreover, the rapid production of dislocations in the structure promotes the tendency for DRX, so that it commonly exceeds DP (Ref 5). This is consistent with the results expressed in Fig. 2.

The absolute solubility temperature of NbC carbides in austenite depends on the concentrations of Nb and C, as follows (Ref 30):

$$\log([\text{Nb}][\text{C}]) = 3.11 - \frac{7520}{T} \quad (\text{Eq 1})$$

where, [Nb] and [C] are the concentration of niobium and carbon in terms of weight percentage, respectively. Using the above equation and the contents of Nb and C (Table 1), the solubility temperature of NbC can be calculated as 1193.66 °C. This temperature also confirms that precipitation of NbC carbides and their interaction with DRX are possible during deformation at the studied temperatures.

### 3.3 Stress Relaxation Results

The stress relaxation test is capable of revealing the starting and finishing times for the strain-induced precipitation at a given deformation temperature (Ref 31, 32). In the obtained stress-time curves (Fig. 5a), three major regions are distinguished (Ref 11). In the first region, stress decreases slightly due to the recovery effect. The drop in stress in the second region is attributed to the conversion of internal elastic stresses into the dislocation movement. In the third region, the stress drop stops due to the start of precipitation (shown by arrows) and the decrease in stress demonstrates the dissolution of precipitates.

The precipitation-recrystallization interaction is possible at all studied deformation temperatures. These observations well comply with the calculation of NbC solubility temperature made by Eq 1. By drawing the precipitation start times (PST) vs. temperature, the precipitation-time-temperature (PTT) diagram has been constructed (Fig. 5b). This curve has a classical C-shape, showing the decrease of PST by enhancing the deformation temperature in range of 900-1050 °C. The PTT curve predicts that PST is minimized at around 1100 °C and then rises again toward infinity at the solution temperature of NbC (1193.66 °C). Indeed, DP is facilitated by an increase in

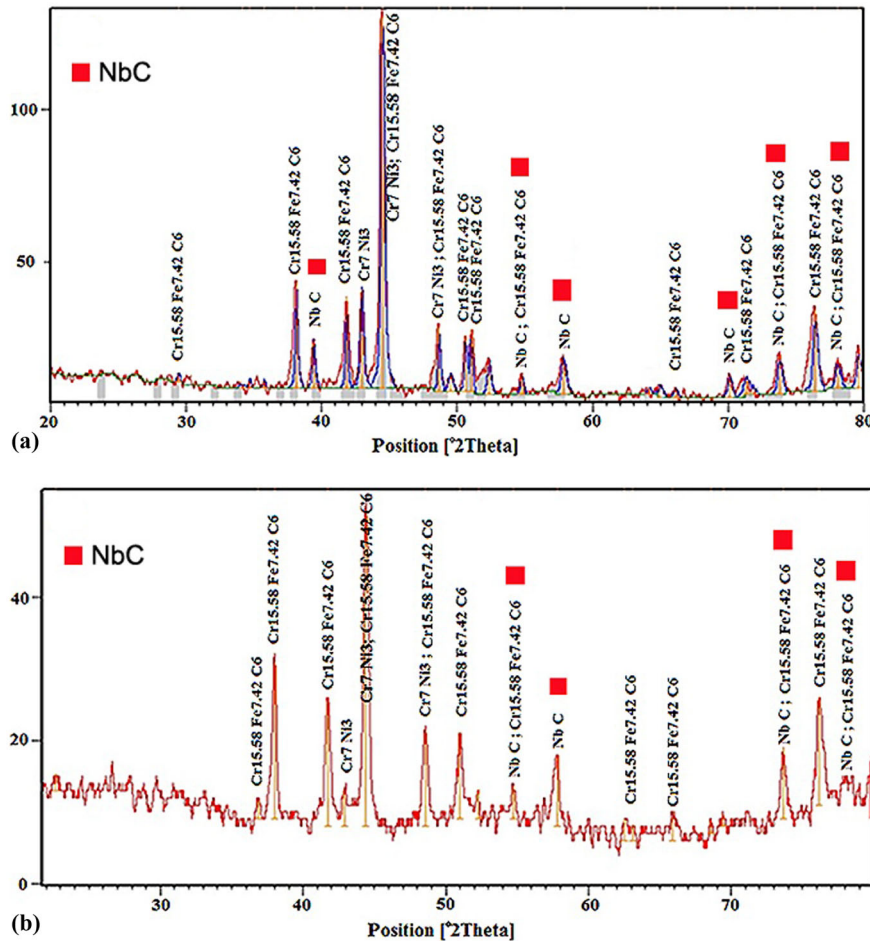


**Fig. 4** X-ray diffraction spectra achieved after electrolytic dissolution. The residues were obtained from the samples compressed at strain rate of  $0.001 \text{ s}^{-1}$  and temperatures of (a)  $900 \text{ }^\circ\text{C}$  and (b)  $1050 \text{ }^\circ\text{C}$

the deformation temperature, indicating the irregular flow behavior of the material at  $950\text{--}1050 \text{ }^\circ\text{C}$ , shown in Fig. 2 and 3(a).

### 3.4 Microstructural Analysis

**3.4.1 Effect of Deformation Temperature.** Figure 6 illustrates the microstructure of samples at strain rate of  $0.001 \text{ s}^{-1}$  and various temperatures. The equiaxial morphology of prior austenite grains at all temperatures indicates that DRX has occurred to some extent depending on the temperature. The simultaneous presence of recrystallized (small) and deformed (large) grains in Fig. 6(b, c and d) implies on the incomplete DRX at  $950\text{--}1050 \text{ }^\circ\text{C}$  with no steady state plateau in the corresponding flow curves (Fig. 2). The incomplete DRX can also be related to the interaction between DP and DRX (proposed in the previous section). As shown by the hot compression and stress relaxation results (Fig. 2, 3a and 5a) and confirmed by the phase analysis data in Fig. 3(b) and 4, at  $950\text{--}1050 \text{ }^\circ\text{C}$ , DP precedes DRX and may retard the recrystallization progress. At  $900 \text{ }^\circ\text{C}$ , however, the PTT curve (Fig. 5b) showed that the PST is long enough to let DRX happens before DP. This prediction is in agreement with the fully recrystallized microstructure in Fig. 6(a).

Figure 6(b) and(c) indicates that DRX has progressed without the formation of a “necklace structure” along the

prior grain boundaries. As the “necklace” is a typical feature along with the DDRX mechanism, it appears that an alternative mechanism should be responsible for the formation of new DRX grains at  $950\text{--}1050 \text{ }^\circ\text{C}$ . In addition, the appearance of some evolving boundaries (highlighted by arrows in Fig. 6(b and c) proposes that CDRX might be the dominant mechanism of microstructural evolution (Ref 33, 34). The idea of CDRX is more corroborated when the role of DP in pinning the original grain boundaries is taken into account. Although austenite is a low-SFE phase and tends to bear DDRX, when it is hindered by fine grain boundary particles, the material is solicited for the alternative mechanism to soften. At this time, DRV extends and joins to CDRX. It is common knowledge that CDRX starts with the progressive growth of sub-grains by the gradual migration of sub-boundaries (Ref 35). These characteristics have also been reported during CDRX in 304 austenitic and duplex stainless steels (Ref 36, 37).

The average grain size for the samples deformed at  $900$ ,  $950$ ,  $1000$  and  $1050 \text{ }^\circ\text{C}$  was determined using the standard intercept method as  $4.56$ ,  $8.17$ ,  $10.07$  and  $24.87 \mu\text{m}$ , respectively. This trend confirms two facts: first, DRX is completed at  $900 \text{ }^\circ\text{C}$  but incomplete at higher temperatures; second, less recrystallization at higher temperatures because of more DP and further grain growth are supportive to the predictions made by the PTT curve, see Fig. 5(b).

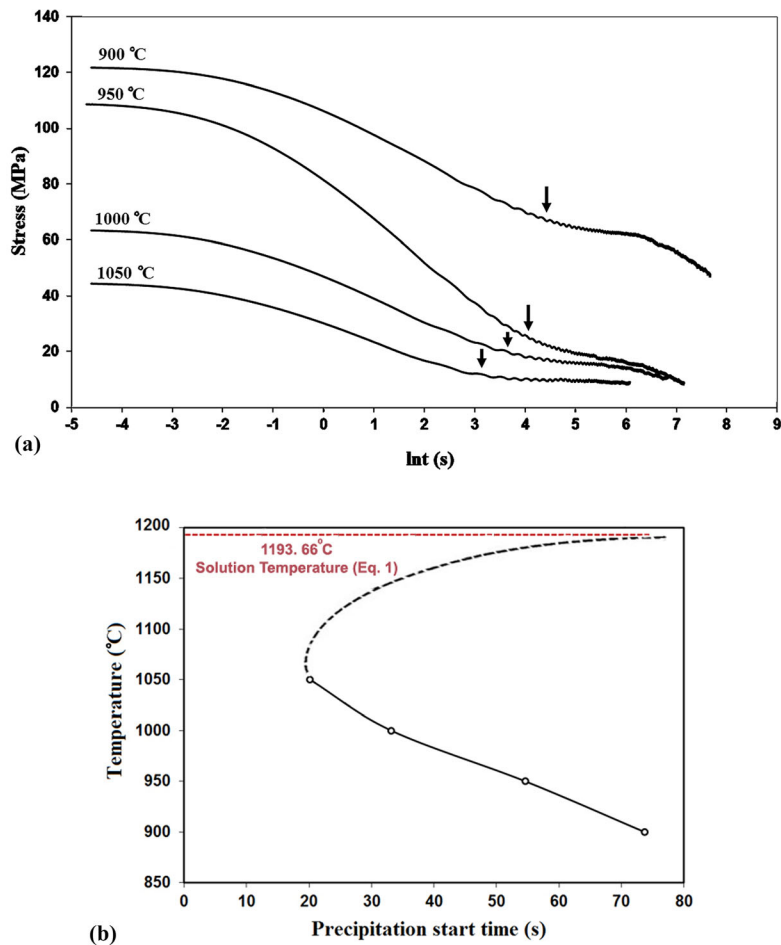


**Fig. 5** (a) Stress relaxation curves at different temperatures. The arrows show the precipitation start times at the deformation temperatures and (b) PTT curve for the precipitation of NbC particles in AISI 630 stainless steel

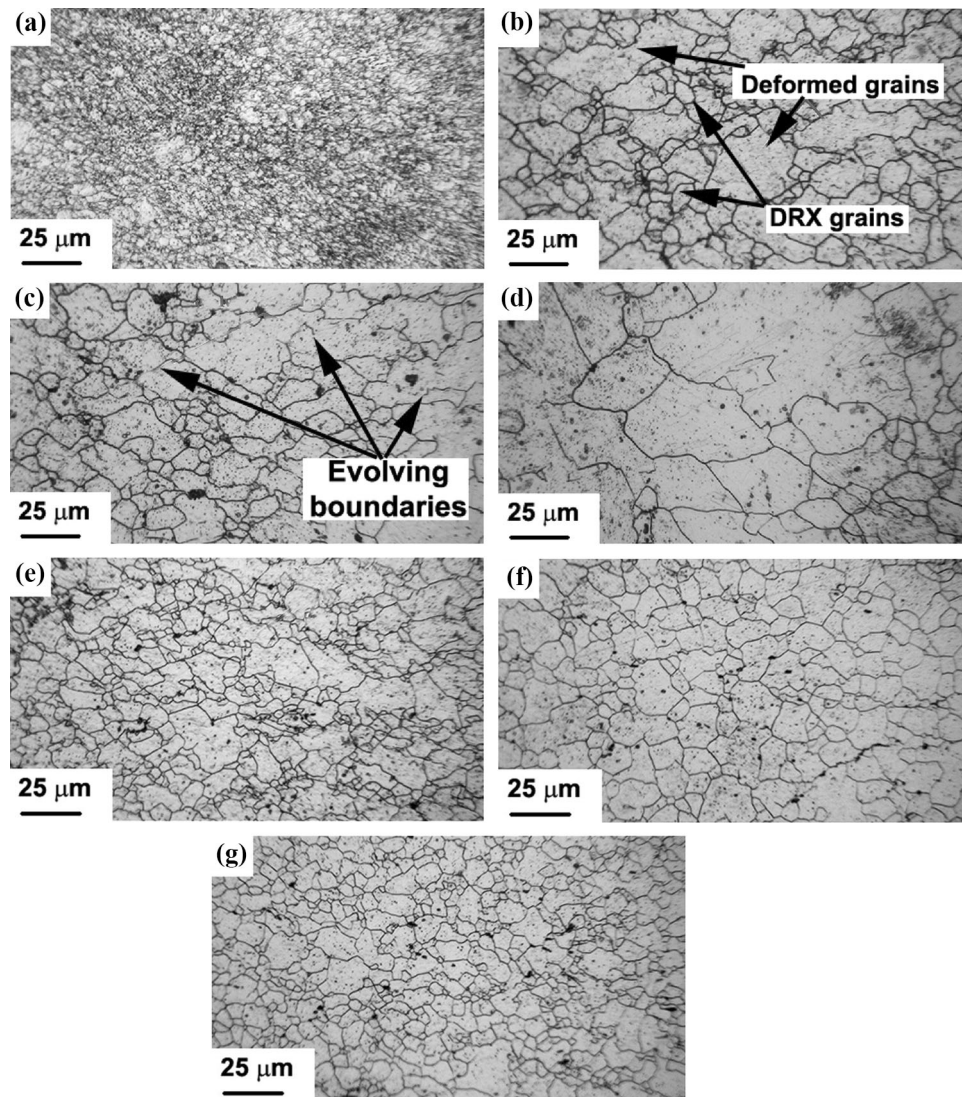
**3.4.2 Effect of Strain Rate.** From the presence of small grains around large grains in Fig. 6(b) and (e), it can be inferred that DRX is still in progress at 950 °C and strain rates of 0.001 and 0.01 s<sup>-1</sup>. However, at 0.1 and 1 s<sup>-1</sup>, Fig. 6(f) and (g), the grain structure is more uniform, showing the complete DRX. The trend of average grain size as 6.12, 7.55 and 5.42 μm, for strain rates of 0.01, 0.1 and 1 s<sup>-1</sup> confirms that DRX has not been completed at low strain rates of 0.001 and 0.1 s<sup>-1</sup>. This is an uncommon behavior because, in general, the opposite effect appears and DRX is completed at low strain rates, where the deformation period is long enough. This anomalous behavior can be again addressed with respect to the feasible interplay between DRX and DP, as evidenced in the prior section. According to the results presented in Fig. 3(a) and 5(a), the temperature of 950 °C lies in the interaction region between DP and DRX. This interaction is more pronounced at lower strain rates, where there is enough deformation period to lead appropriate amount of fine particles at the original grain boundaries. While at high strain rates (i.e., 0.1 and 1 s<sup>-1</sup>) the deformation time is shorter than required to occur enough DP. Hence, DRX happens freely and a more uniform microstructure is obtained.

Figure 7 demonstrates the SEM micrographs of samples deformed at 1050 °C and strain rates of 0.001 and 0.1 s<sup>-1</sup>.

Figure 7(a) and (b) exhibits fine precipitates inside the grains and at the grain boundaries. According to the EDS analysis presented in Fig. 7(c), the fine particles mainly perceived at the boundaries are NbC carbides with an average size of 100-200 nm. The presence of NbC on the grain boundaries (denoted by arrows) supports the previous results and confirms the interaction between DRX and DP at high temperatures.

**3.4.3 EBSD Observations.** Figure 8 shows the inverse pole figures (IPFs) and grain boundary maps (GBMs) of samples deformed at different strains. A comparison between the GBMs in Fig. 8(b) and (d) suggests the formation of further DRX grains with the increase in strain from 0.3 to 0.7 at 950 °C and 0.01 s<sup>-1</sup>. The same result is elicited from the IPFs in Fig. 8(a) and (c), showing the gradual progress of DRX so that it only leads to a very slight flow softening as observed in Fig. 2(b). Too many incomplete HAGBs (colored black) joint to LAGBs (shown by arrows) infer that DRX is taking place through the gradual evolution of LAGBs into HAGBs. As discussed before, this is the general characteristic of the CDRX process (Ref 38, 39). These observations are consistent with the optical micrograph in Fig. 6(e), which showed DRX fine grains with only a few larger old grains after the strain of 0.7. Meanwhile, Fig. 8(e) and (f) exhibits the typical EBSD-GBM





**Fig. 6** Microstructure of samples deformed at strain rate of  $0.001 \text{ s}^{-1}$  and temperatures of (a)  $900 \text{ }^\circ\text{C}$ , (b)  $950 \text{ }^\circ\text{C}$ , (c)  $1000 \text{ }^\circ\text{C}$ , (d)  $1050 \text{ }^\circ\text{C}$ ; at  $950 \text{ }^\circ\text{C}$  and strain rates of (e)  $0.01 \text{ s}^{-1}$ , (f)  $0.1 \text{ s}^{-1}$  and (g)  $1 \text{ s}^{-1}$ .

results from the samples deformed at different temperatures and strain rates. A comparison between Fig. 8(d) and (e) indicates that the increase in strain rate from  $0.01$  to  $0.1 \text{ s}^{-1}$  (at  $950 \text{ }^\circ\text{C}$  to a strain of  $0.7$ ) has promoted the DRX. More HAGB, less LAGB and more uniform grain structure with regular grain boundaries are all signs of more progressed DRX. However, there are some incomplete grain boundaries, shown by arrows, which imply that DRX is not fully completed yet. Shorter deformation time at  $0.1 \text{ s}^{-1}$  and therefore less DP can be responsible for the further progress of DRX. Figure 8(f) shows the lower volume fraction of HAGBs with respect to LAGBs, indicating sluggish DRX at temperature of  $1050 \text{ }^\circ\text{C}$  and strain rate of  $0.01 \text{ s}^{-1}$ . In other words, DRV can be introduced as the dominant softening mechanism. This is contrary to our expectation to have further DRX at higher temperatures. As mentioned in the former section and confirmed by the PTT curves in Fig. 5(b), these unusual behavior can be attributed to the interplay between DP and DRX. The NbC particles formed

by DP interact with DRX in the temperature range of  $950$ - $1050 \text{ }^\circ\text{C}$ . They actually pin the grain boundaries and therefore postpone DRX. The PTT curve showed that the PST for DP is considerably reduced with an increase in the deformation temperature; and this leads to the formation of more NbC particles at the grain boundaries. The DRX at  $1050 \text{ }^\circ\text{C}$  is more delayed by DP comparing to the lower temperatures, such as  $950 \text{ }^\circ\text{C}$ . In the absence of DRX, DRV proceeds inevitably toward CDRX at larger strains. This can also explain why the corresponding flow curves in Fig. 2(d) show a long plateau with weak flow softening.

The typical results of pole figure and ODF analyses of deformed samples have been demonstrated in Fig. 9. It appears that in the specimen deformed to the true strain of  $0.7$  at temperature of  $1050 \text{ }^\circ\text{C}$  and strain rate of  $0.01 \text{ s}^{-1}$ , texture is nearly random with some bias to the Brass  $\{110\} \langle 12 \rangle$ , Goss  $\{110\} \langle 001 \rangle$  and the Copper  $\{112\} \langle 11 \rangle$  components, Fig. 9(a). These components are generally observed in

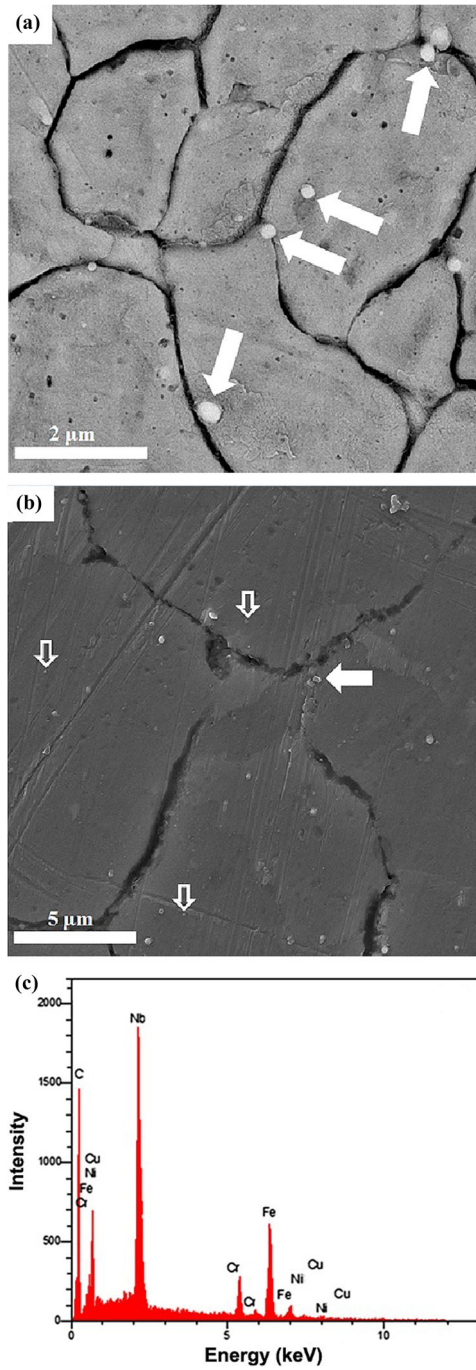


**Fig. 7** SEM micrographs of samples deformed at 1050 °C and strain rates of (a) 0.001 s<sup>-1</sup>, (b) 0.1 s<sup>-1</sup> and (c) EDX of the precipitates presented in (a)

hot deformed FCC metals (Ref 40). The texture developed in the sample deformed at 950 °C–0.1 s<sup>-1</sup> has been exhibited in Fig. 9(b). It is evident that near-Cube {001} <100> and Rotated Cube {001} <110> are the dominant texture components, which are typical of DRX. The ODFs in the  $\varphi_2 = 0^\circ$  and  $45^\circ$ , Fig. 9(e) and (f) suggest that texture evolution can be influenced by temperature and strain rate due to the acceleration of precipitation formation and deceleration of DRX. There is a distinct texture with the corresponding peak intensity of 7.864 when the deformation temperature is low. Also, when the stored energy is large enough to form a large fraction of DRX at

higher temperature, the relative peak intensity is remained nearly unchanged,  $7.932 \times R$  (Fig. 9 e, f). On the other hand, in several alloys, it has been reported that DRX may weaken the texture (Ref 41, 42). This contradiction might be ascribed to the recrystallization texture along with CDRX (Ref 43).

### 3.5 Constitutive Analysis

Constitutive equations for describing the effect of variables on flow stress are widely used through the numerical modeling of hot working processes (Ref 44). The Zener–Hollomon parameter has been proposed to express the combined effect of strain rate and temperature on the flow stress of metals (Ref 5):

$$Z = \dot{\epsilon} \exp\left(\frac{Q_{\text{def}}}{RT}\right) \quad (\text{Eq 2})$$

where,  $Q_{\text{def}}$  is the activation energy,  $R$  is the universal gas constant and  $T$  is the absolute temperature. The most commonly used constitutive equations are the exponential, the power-law and the hyperbolic sine functions presented as follows (Ref 45–47):

$$Z = \dot{\epsilon} \exp\left(\frac{Q_{\text{def}}}{RT}\right) = A[\sinh(\alpha\sigma)]^n \quad (\text{Eq 3})$$

$$Z = \dot{\epsilon} \exp\left(\frac{Q_{\text{def}}}{RT}\right) = A'\sigma^{n'} \quad (\text{Eq 4})$$

$$Z = \dot{\epsilon} \exp\left(\frac{Q_{\text{def}}}{RT}\right) = A'' \exp(\beta\sigma) \quad (\text{Eq 5})$$

where,  $A$ ,  $A'$ ,  $A''$ ,  $n$ ,  $n'$ ,  $\alpha$  and  $\beta$  are the constants. As shown in the above equations, the  $Z$  parameter clearly correlates with the flow stress. This means, when the temperature increases or strain rate decreases, the  $Z$  parameter and flow stress is reduced. This can be observed in the experimental flow curves in Fig. 2. Taking natural logarithm of Eq 3, 4 and 5 leads to:

$$\ln[\sinh(\alpha\sigma)] = \frac{1}{n} \ln \dot{\epsilon} + \frac{1}{n} \left(\frac{Q_{\text{def}}}{RT}\right) - \frac{1}{n} \ln A \quad (\text{Eq 6})$$

$$\ln \sigma = \frac{1}{n'} \ln \dot{\epsilon} + \frac{1}{n'} \left(\frac{Q_{\text{def}}}{RT}\right) - \frac{1}{n'} \ln A' \quad (\text{Eq 7})$$

$$\sigma = \frac{1}{\beta} \ln \dot{\epsilon} + \frac{1}{\beta} \left(\frac{Q_{\text{def}}}{RT}\right) - \frac{1}{\beta} \ln A'' \quad (\text{Eq 8})$$

The subsequent equations can be written by the partial differentiation of Eq 6, 7 and 8:

$$n = \frac{d(\ln \dot{\epsilon})}{d\{\ln[\sinh(\alpha\sigma)]\}} \quad (\text{Eq 9})$$

$$n' = \frac{d(\ln \dot{\epsilon})}{d(\ln \sigma)} \quad (\text{Eq 10})$$

$$\beta = \frac{d(\ln \dot{\epsilon})}{d(\sigma)} \quad (\text{Eq 11})$$

The plots of  $\ln \sigma - \ln \dot{\epsilon}$  and  $\sigma - \ln \dot{\epsilon}$  for the typical strain of 0.4 are illustrated in Fig. 10. The mean of slopes in Fig. 10(a)



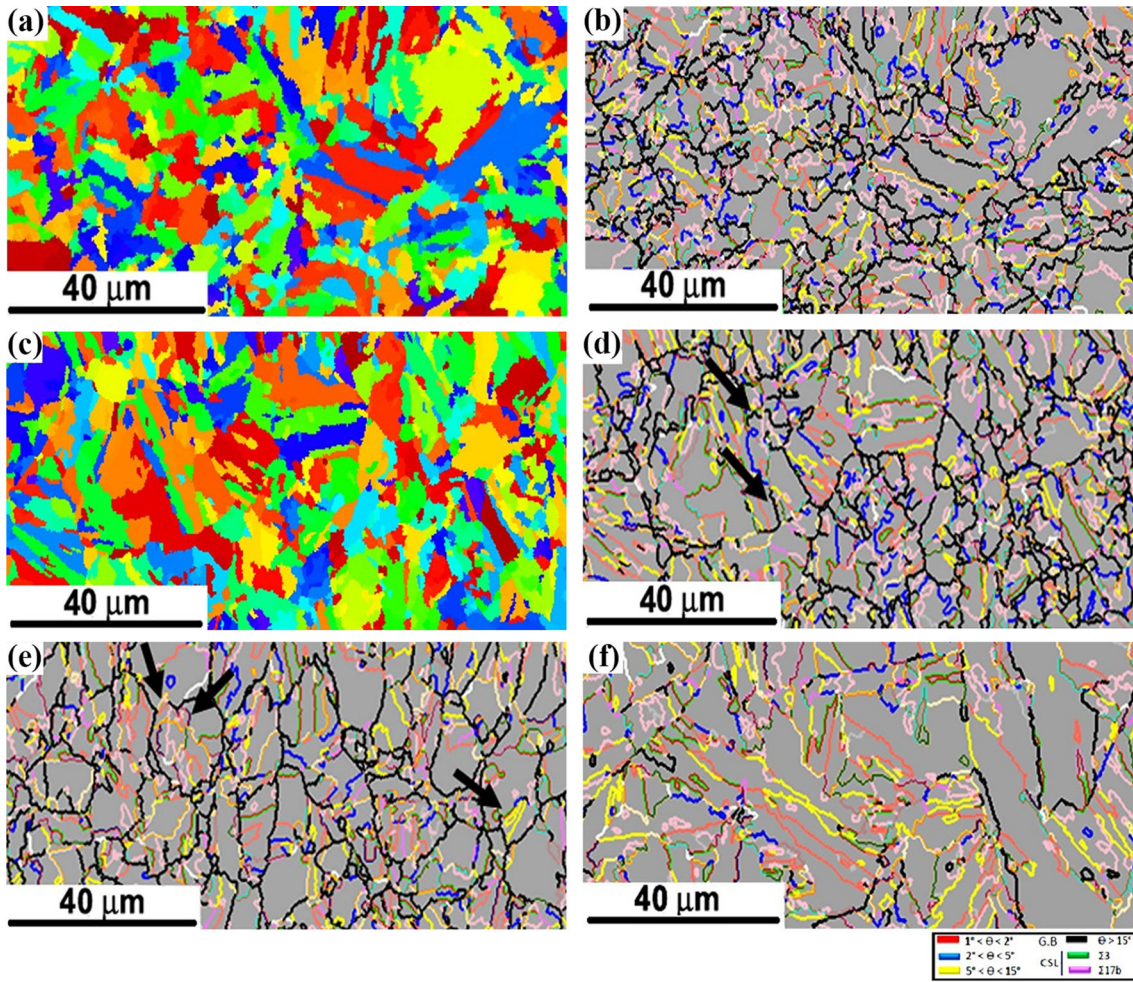


**Fig. 8** EBSD images of the samples deformed to strains of (a, b) 0.3 and (c, d) 0.7 at temperature of 950 °C and strain rate of 0.01 s<sup>-1</sup>; EBSD images obtained at a strain of 0.7 and typical conditions of (e) 950 °C/ 0.1 s<sup>-1</sup> and (f) 1050 °C/ 0.01 s<sup>-1</sup>. (a, c) represent the inverse pole figures and (b, d, e, f) exhibit the grain boundary maps

and (b) gives the values of  $\frac{1}{n}$  and  $\frac{1}{\beta}$  as 0.1616 and 11.7493, respectively.

Finally, the amount of stress coefficient in Eq 3 is achieved equal to  $\alpha = 0.0138$  ( $= \beta/\beta'$ ) (Ref 45-47). According to Eq 9, the value of  $n$  is assessed by finding the average slope of lines in the plot of  $\ln \dot{\epsilon}$  vs.  $\ln[\sinh(\alpha\sigma)]$ , as shown in Fig. 11(a). Also, the activation energy can be determined by partial differentiation of Eq 6:

$$Q_{\text{def}} = Rn \frac{d\{\ln[\sinh(\alpha\sigma)]\}}{d(\frac{1}{T})} \quad (\text{Eq 12})$$

Figure 11(b) indicates the changes in flow stress versus reciprocal temperature. The term  $\partial\{\ln[\sinh(\alpha\sigma)]\}/\partial(1/T)$  is assessed via mean slope at various strain rates ( $\approx 1.3146$ ). Then, the amount of  $Q_{\text{def}}$  is obtained as 485.59 kJ/mol. This value is in good agreement with the  $Q_{\text{def}}$  values published in the literature for other stainless steels (Ref 48-50).

The value of  $A$  can be determined by taking natural logarithm from both sides of Eq 3:

$$\ln Z = \ln A + n \ln[\sinh(\alpha\sigma)] \quad (\text{Eq 13})$$

Therefore, the parameter  $A$  can be achieved using the intercept in  $\ln Z$  vs.  $\ln[\sinh(\alpha\sigma)]$  plot (Fig. 11c). By replacement

of the calculated constants, the hyperbolic sine equation for AISI 630 stainless steel is given by:

$$Z = \dot{\epsilon} \exp\left(\frac{485590}{RT}\right) = 9.81 \times 10^{17} [\sinh(0.0138 \sigma)]^{4.44} \quad (\text{Eq 14})$$

The  $Q_{\text{def}}$  gives the average value of energy dissipated per mole of material, at the deformation interval. By the same method, the value of  $Q_i$  at each pair of temperature and strain rate ( $T_i, \epsilon_i$ ) can be determined. As  $Q_i$  reflects the deformation resistance, its calculation can help to better analyze the underlying microstructural mechanisms at ( $T_i, \epsilon_i, \dot{\epsilon}_i$ ). For this purpose, the discrete form of Eq 9 and 12 can be written as follows:

$$n_i = \frac{\ln \epsilon_{i+1} - \ln \epsilon_i}{\ln[\sinh(\alpha\sigma_{i+1})] - \ln[\sinh(\alpha\sigma_i)]}$$

$$Q_i = Rn_i \frac{\ln[\sinh(\alpha\sigma_{i+1})] - \ln[\sinh(\alpha\sigma_i)]}{(1/T_{i+1}) - (1/T_i)} \quad (\text{Eq 15})$$

The map of  $Q_i$  in the form of 3-D and 2-D (contour map) diagrams is shown in Fig. 12. According to this figure, the maximum amount of activation energy is in two ranges of:

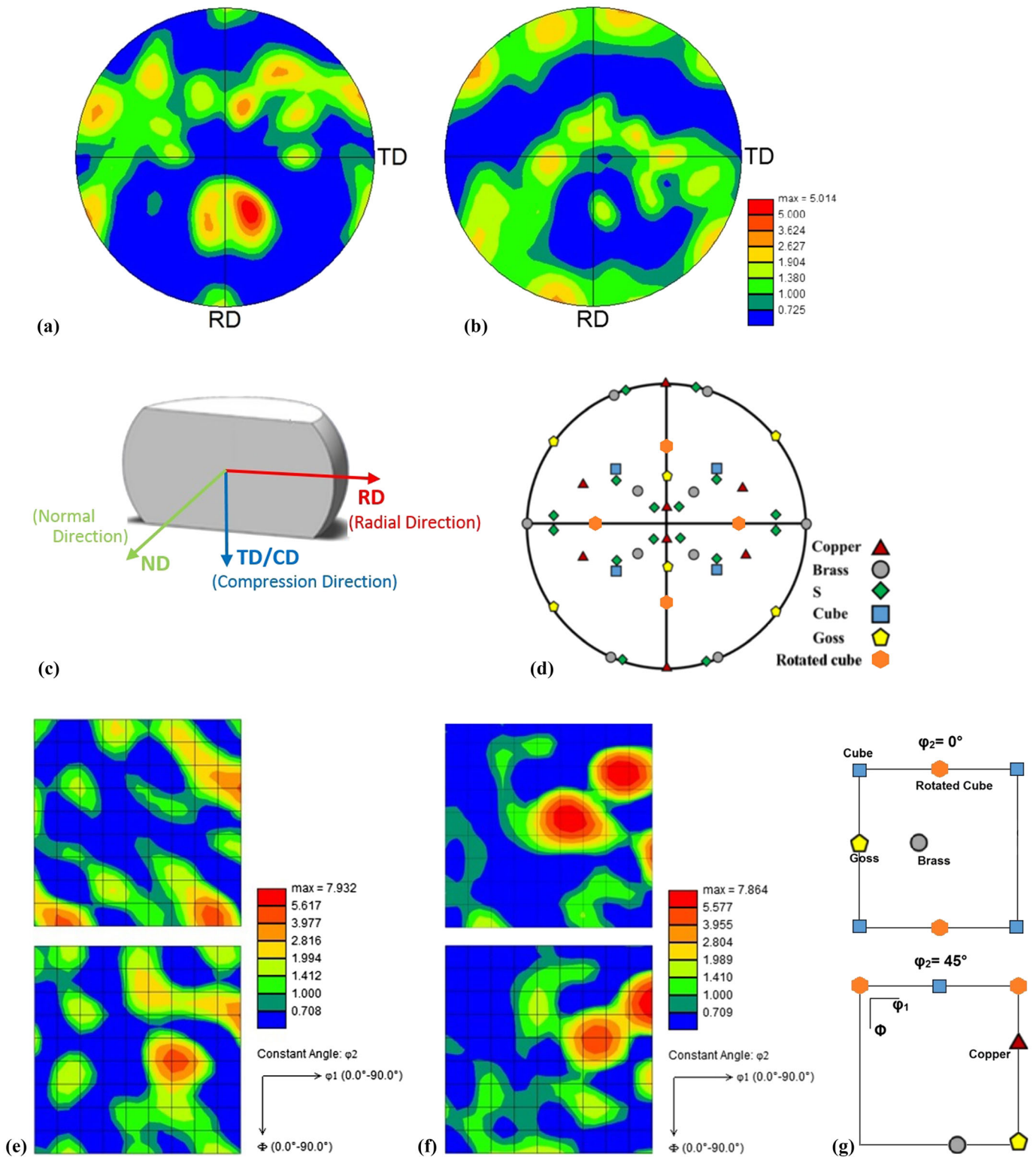


**Fig. 9** The  $\{111\}$  pole figures and  $\phi_2 = 0^\circ$  and  $45^\circ$  ODF sections of samples subjected to compression under different conditions: (a, e) strain of 0.3, strain rate of  $0.01 \text{ s}^{-1}$  and temperature of  $1050 \text{ }^\circ\text{C}$ , (b, f) strain of 0.7, strain rate of  $0.1 \text{ s}^{-1}$  and temperature of  $950 \text{ }^\circ\text{C}$ , (c, d, g) schematic illustration of the sample frame of reference, typical orientations of a FCC material in (111) pole figure and ODF

$950 \text{ }^\circ\text{C}$  and low strain rates; and  $950\text{-}1000 \text{ }^\circ\text{C}$  and medium strain rates. This result is consistent with the observations regarding the DP of NbC particles and their interaction with DRX, presented in Fig. 3(a), 5, 6 and 8. Current observations

reveal that the NbC formation increases the deformation resistance of material, presumably due to the delay in DRX and its interplay with the matrix dislocations.



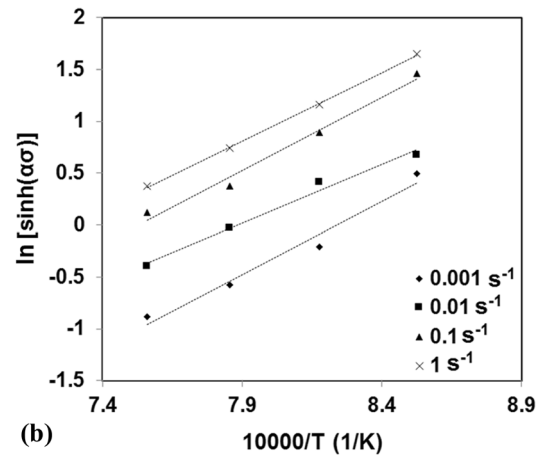
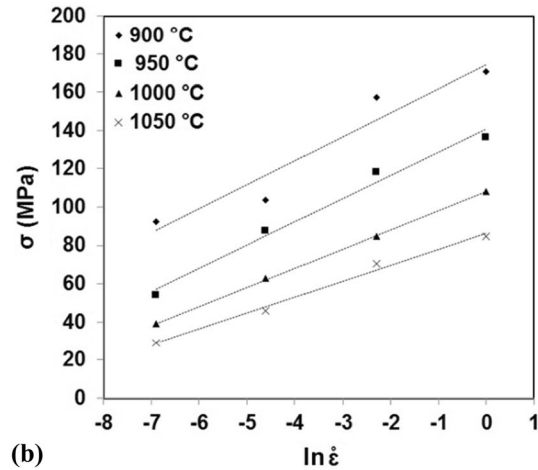
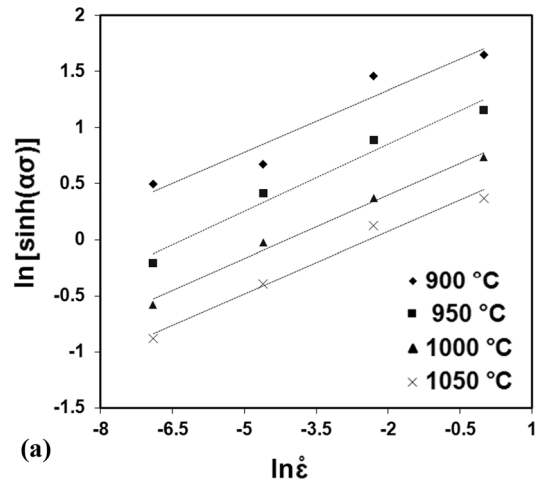
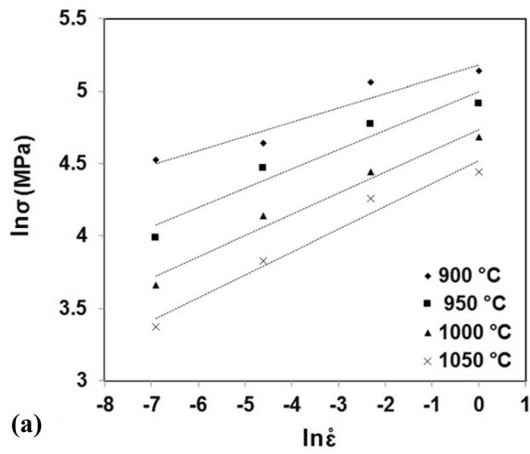


**Fig. 10** Relationships between flow stress and strain rate at typical strain of 0.4: (a) log-log window for calculating  $n'$  (stress exponent, Eq 4) and (b) semi-log window to determine  $\beta$  (coefficient of stress, Eq 5)

## 4. Conclusion

Hot compression tests were performed on AISI 630 stainless steel in the temperature range of 900-1050 °C and the strain rates of 0.001-1 s<sup>-1</sup>. The major results of this research are as follows:

1. Single peak flow behavior was observed at all deformation conditions. The peak stress is increased with rise in strain rate and decline in temperature. The flow curves were specified by a faint peak and slight flow softening which assigned as continuous dynamic recrystallization.
2. XRD analysis of the residue obtained from the electrolytic extraction of samples showed that NbC and Cr<sub>15.58</sub>Fe<sub>7.42</sub>C<sub>6</sub> (M<sub>23</sub>C<sub>6</sub>) are the major precipitates in the deformed samples.
3. The stress relaxation tests exhibited that dynamic precipitation of NbC can interact with DRX in the range between 950 and 1050 °C; and the precipitation start time decreases with increasing temperature consistent with the irregular variation of peak strain.
4. By applying the hyperbolic sine constitutive equation, the amount of activation energy was assigned as 485.59 kJ/mol. The maps of activation energy in the tem-

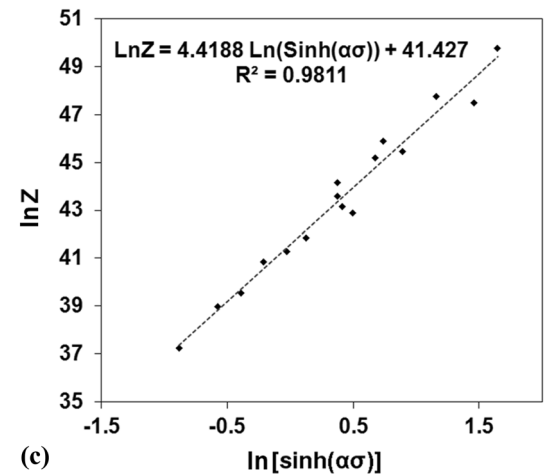


**Fig. 11** The dependence of hyperbolic sine function of flow stress on (a) strain rate, (b) the reciprocal of deformation temperature and (c) the dependence of  $\ln Z$  on the hyperbolic sine function of flow stress at the typical strain of 0.4

perature-strain rate window showed that the precipitation of NbC leads to increase in the deformation resistance of material.

5. EBSD observations confirmed that CDRX occurs by the developing transformation of sub-boundaries into high angle grain boundaries. In addition, DRX was found to



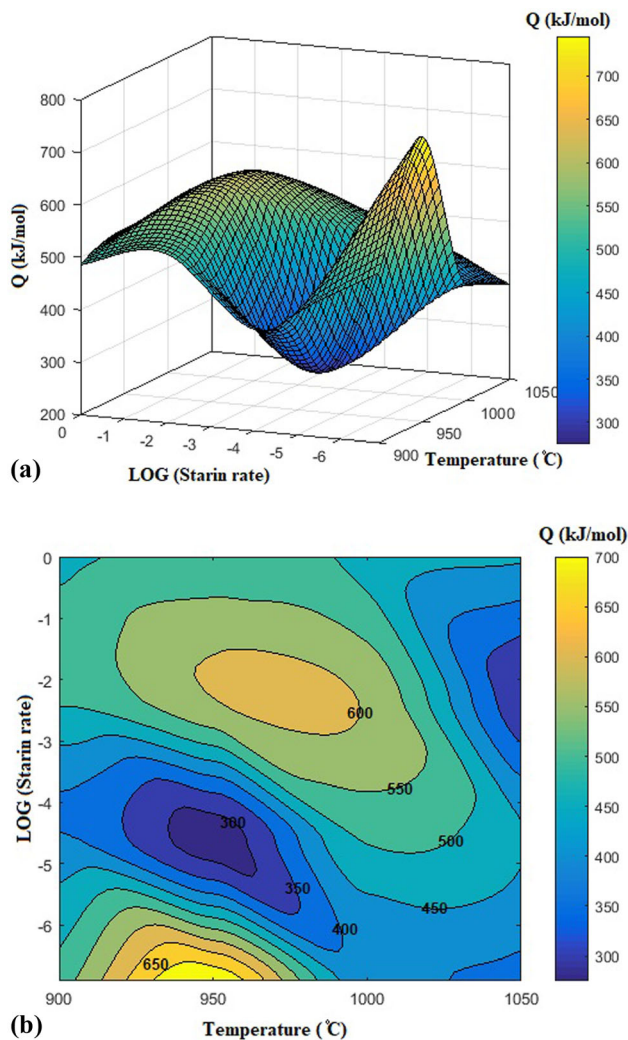


**Fig. 12** (a) 3-D and (b) 2-D windows of the activation energy ( $Q$ ) at the typical strain of 0.4

be less developed at higher deformation temperatures due to the dynamic precipitation.

- The strong Brass, Goss and Copper components were achieved via grains rotation through hot deformation process shifting to the recrystallization texture after DRX. The intensity of texture components remains unchanged, indicating that the CDRX is likely to occur.

## References

- V.H. Lara, L.G. Fuentes, O.C. Alvarado, A.S. Rodriguez, and E.G. Sanchez, Hot Ductility of the 17-4 PH Stainless Steels, *J. Mater. Eng. Perform.*, 2016, **25**, p 1041–1046.
- J.C.M. Farrar, *The alloy tree: A guide to low-alloy steels, stainless steels and nickel-base alloys*, Woodhead Publishing, Cambridge, 2004
- H. Mirzadeh, A Simplified Approach for Developing Constitutive Equations for Modeling and Prediction of Hot Deformation Flow Stress, *Metall. Mater. Trans. A*, 2015, **46**, p 4027–4037.
- A. Momeni and K. Dehghani, Characterization of hot Deformation Behavior of 410 Martensitic Stainless Steel Using Constitutive Equations and Processing Maps, *Mater. Sci. Eng. A*, 2010, **527**, p 5467–5473.

- F.J. Humphreys and M. Hatherly, *Recrystallization and related annealing phenomena*, 2nd ed. Elsevier, Oxford, 2004
- K. Morsi, J. Wall, J. Rodriguez, and S.O. Moussa, Reactive Thermo-mechanical Processing of Intermetallic Materials, *J. Mater. Eng. Perform.*, 2003, **12**, p 147–156.
- N. Bibhanshu, A. Bhattacharjee, and S. Suwas, Hot Deformation Response of Titanium Aluminides Ti-45Al-(5,10)Nb-0.2B-0.2C with Pre-Conditioned Microstructures, *J. Alloys Compd.*, 2020, **832**, p 154584.
- G.R. Ebrahimi, H. Keshmiri, A. Momeni, and M. Mazinani, Dynamic Recrystallization Behavior of a Superaustenitic Stainless Steel Containing 16%Cr and 25%Ni, *Mater. Sci. Eng. A*, 2011, **528**, p 7488–7493.
- X. Wang, B. Shen, L. Deng, and J. Li, Effects of Original Orientation Combination on Substructure Characteristics During Continuous Dynamic Recrystallization in an Extruded Al Cu-Li Alloy, *Mater. Charact.*, 2017, **130**, p 113–122.
- A. Momeni, S.M. Abbasi, M. Mobarakabati, and H. Badri, A Comparative Study on the Hot Working Behavior of INCONEL 718 and ALLVAC 718 Plus, *Metall. Mater. Trans. A*, 2017, **48**, p 1216–1229.
- G.R. Ebrahimi, A. Momeni, M. Jahazi, and P. Bocher, Dynamic Recrystallization and Precipitation in 13Cr Super-Martensitic Stainless Steels, *Metall. Mater. Trans. A*, 2014, **45**, p 2219–2231.
- J.J. Jonas, Mechanical Testing for the Study of Austenite Recrystallization and Carbonitride Precipitation, Proceedings of the International Conference of HSLA steels, University of Wollongong, Australia, 80–89, 1984
- D. Weygand, Y. Brechet, and J. Leapinoux, Zener Pinning and Grain Growth: A Two-Dimensional Vertex Computer Simulation, *Acta Mater.*, 1999, **47**, p 961–970.
- M. Mirzaee, H. Keshmiri, G.R. Ebrahimi, and A. Momeni, Dynamic Recrystallization and Precipitation in Low Carbon Low Alloy Steel 26NiCrMoV 14-5, *Mater. Sci. Eng. A*, 2012, **551**, p 25–31.
- A. Momeni and K. Dehghani, Microstructural Evolution and Flow Analysis During Hot Working of A Fe-Ni-Cr Superaustenitic Stainless Steel, *Metall. Mater. Trans. A*, 2011, **42**, p 1925–1932.
- Z. Zeng, L. Chen, F. Zhu, and X. Liu, Static Recrystallization Behavior of a Martensitic Heat-Resistant Stainless Steel 403Nb, *Acta Metall. Sin.*, 2011, **24**, p 381–389.
- W.J. Liu and J.J. Jonas, A Stress Relaxation Method for Following Carbonitride Precipitation in Austenite at Hot Working Temperatures, *Metall. Trans.*, 1988, **19**, p 1403–1413.
- R.A. Abrahams, *The development of high strength corrosion resistant precipitation hardening cast steels*, The Pennsylvania State University, Pennsylvania, 2010
- A.S. Murthy, *Role of alloy additions on strengthening in 17-4 PH stainless steel, doctoral dissertations*, Missouri University of Science and Technology, Missouri, 2013
- R.D. Doherty, D.A. Hughes, F.J. Humphreys, and J.J. Jonas, Current Issues in Recrystallization: A Review, *Mater. Sci. Eng.*, 1997, **238**, p 219–274.
- Y.C. Lin and X. Chen, A Critical Review of Experimental Results and Constitutive Descriptions for Metals and Alloys in Hot Working, *Mater. Des.*, 2011, **32**, p 1733–1759.
- Y. Han, Y. Sun, W. Zhang, and H. Chen, Hot Deformation and Processing Window Optimization of a 70MnSiCrMo Carbide-Free Bainitic Steel, *Mater.*, 2017, **10**, p 318.
- T. Saka, A. Belyakov, R. Kaibyshev, H. Miura, and J.J. Jonas, Dynamic and Post-Dynamic Recrystallization Under Hot, Cold and Severe Plastic Deformation Conditions, *Prog. Mater. Sci.*, 2014, **60**, p 130–207.
- H. Mirzadeh, J.M. Cabrera, and A. Najafizadeh, Constitutive Relationships for Hot Deformation of Austenite, *Acta Mater.*, 2011, **59**, p 6441–6448.
- A. Momeni, K. Dehghani, G.R. Ebrahimi, and H. Keshmiri, Modeling the Flow Curve Characteristics of 410 Martensitic Stainless Steel under Hot Working Condition, *Met. Mater. Trans. A*, 2010, **41**, p 2898–2904.
- Z. Yao, H. Wang, J. Dong, J. Wang, H. Jiang, and B. Zhou, Characterization of Hot Deformation Behavior and Dislocation Structure Evolution of an Advanced Nickel-Based Superalloy, *Metals*, 2020, **10**(p920), p 1p.

27. G.R. Ebrahimi, A. Momeni, Sh. Kazemi, and H. Alinejad, Flow Curves, Dynamic Recrystallization and Precipitation in A Medium Carbon Low Alloy Steel, *Vac.*, 2017, **142**, p 135–145.
28. H.J. McQueen and J.J. Jonas, Recent Advances in Hot Working: Fundamental Dynamic Softening Mechanisms, *J. Appl. Metalwork.*, 1984, **3**(3), p 233–241.
29. N. Radovic, Correlation Between Apparent Activation Energy for Hot Working and Temperature of no Recrystallization In Microalloyed Steels, *Mater. Sci. Forum.*, 2003, **426–432**, p 1553–1558.
30. M.F. Ashby and K.E. Easterlig, A First Report on Diagrams for Grain Growth in Welds, *Acta metal.*, 1982, **30**, p 1969–1978.
31. M. Jahazi, H. Monajati, F. Zarandi, and S. Yue, Strain Induced Gamma Prime Precipitation in Ni-Based Superalloy Udimet 720 Using A Stress Relaxation Based Technique, *Scr. Metal. Mater.*, 2005, **52**, p 771–776.
32. S.S. Hansen, J.B.V. Sande, and M. Cohen, Niobium Carbonitride Precipitation and Austenite Recrystallization in Hot-Rolled Microalloyed Steel, *Metal. Trans.*, 1980, **11**, p 387–402.
33. N. Prasad, N. Bibhanshu, N. Nayan, G.S. Avadhani, and S. Suwas, Hot Deformation Behavior of the High-Entropy Alloy CoCuFeMnNi, *J. Mater. Res.*, 2019, **34**, p 744–755.
34. B. Eghbali, Effect of Strain Rate on the Microstructural Development Through Continuous Dynamic Recrystallization in A Microalloyed Steel, *Mater. Sci. Eng. A*, 2010, **527**, p 3402–3406.
35. Z. SangariMotlagh, B. Tolaminejad, and A. Momeni, Prediction of Hot Deformation Flow Curves of 1.4542 Stainless Steel, Prediction of Hot Deformation Flow Curves of 1.4542 Stainless Steel, *Metal. Mater. Int.*, 2021, **27**, p 2512–2529.
36. Z. Yanushkevich, A. Belyakov, and R. Kaibyshev, Microstructural Evolution of A 304-Type Austenitic Stainless Steel During Rolling at Temperatures of 773-1273 K, *Acta Mater.*, 2015, **82**, p 244–254.
37. K. Tsuzaki, H. Xiaoxu, and T. Maki, Mechanism of Dynamic Continuous Recrystallization During Superplastic Deformation in A Microduplex Stainless Steel, *Acta mater.*, 1996, **44**, p 4491–4499.
38. G.R. Ebrahimi, A. Momeni, H.R. Ezatpour, M. Jahazi, and P. Bocher, Dynamic Recrystallization in Monel400 Ni-Cu Alloy: Mechanism and Role of Twinning, *Mater. Sci. Eng. A*, 2019, **744**, p 376–385.
39. C. Liao, H. Wu, C. Wu, F. Zhu, and S. Lee, Hot Deformation Behavior and Flow Stress Modeling of Annealed AZ61 Mg Alloys, *Prog. Nat. Sci. Mater. Int.*, 2014, **24**, p 253–265.
40. L. Bracke, K. Verbeken, L. Kestens, and J. Penning, Microstructure and Texture Evolution During Cold Rolling and Annealing of A High Mn TWIP Steel, *Acta Mater.*, 2009, **57**, p 1512–1524.
41. I.S. Wani, G.D. Sathiaraj, M.Z. Ahmed, S.R. Reddy, and P.P. Bhattacharjee, Evolution of Microstructure and Texture During Thermo-Mechanical Processing of A Two Phase Al0.5CoCrFeMnNi High Entropy Alloy, *Mater. Charact.*, 2016, **118**, p 417–424.
42. A.M. Wusatowska-Sarnek, H. Miura, and T. Sakai, Nucleation and Microtexture Development Under Dynamic Recrystallization of Copper, *Mater. Sci. Eng. A*, 2002, **323**, p 177–186.
43. Z. Huang, Z. Lu, S. Jiang, Ch. Wang, and K. Zhang, Dynamic Recrystallization Behavior and Texture Evolution of NiAl Intermetallic During Hot Deformation, *J. Mater. Eng. Perform.*, 2017, **26**(5), p 2377–2387.
44. C. Zener and J.H. Hollomon, Effect of Strain Rate Upon Plastic Flow of Steel, *J. Appl. Phys.*, 1944, **15**, p 22–32.
45. C.M. Sellars and W.J. McG, Tegart, Hot Workability, *Int. Metall. Rev.*, 1972, **17**, p 1–24.
46. F. Garofalo, *Fundamental of creep and creep-rupture in metals*, Macmillan, University of California, 1965
47. A. Momeni, A. Shokuhfar, and S.M. Abbasi, Dynamic Recrystallization of A Cr-Ni-Mo-Cu-Ti-V Precipitation Hardenable Stainless Steel, *J. Mater. Sci. Technol.*, 2007, **23**, p 775–778.
48. K.A. Babu and S. Mandal, Regression Based Novel Constitutive Analyses to Predict High Temperature Flow Behavior in Super Austenitic Stainless Steel, *Mater. Sci. Eng. A*, 2017, **703**, p 187–195.
49. M. Aghaie-Khafri and F. Adhami, Hot Deformation of 15-5 PH Stainless Steel, *Mater. Sci. Eng. A*, 2010, **527**(4–5), p 1052–1057.
50. Y.C. Lin, M.S. Chen, and J. Zhong, Constitutive Modeling for Elevated Temperature Flow Behavior of 42CrMo Steel, *Comput. Mater. Sci.*, 2008, **42**, p 470–477.

**Publisher's Note** Springer Nature remains neutral with regard to jurisdictional claims in published maps and institutional affiliations.